

1

²A SEARCH FOR LONG-LIVED, CHARGED, SUPERSYMMETRIC PARTICLES
³USING IONIZATION WITH THE ATLAS DETECTOR

4

BRADLEY AXEN

5

September 2016 – Version 0.23

6



⁸ Bradley Axen: *A Search for Long-Lived, Charged, Supersymmetric Particles using Ion-
⁹ ization with the ATLAS Detector*, Subtitle, © September 2016

¹⁰

Usually a quotation.

¹¹

Dedicated to.

₁₂ ABSTRACT

₁₃ How to write a good abstract:

₁₄ <https://plg.uwaterloo.ca/~migod/research/beck00PSLA.html>

₁₅ PUBLICATIONS

₁₆ Some ideas and figures have appeared previously in the following publications:

₁₇

₁₈ Put your publications from the thesis here. The packages `multibib` or `bibtopic`
₁₉ etc. can be used to handle multiple different bibliographies in your document.

²¹ ACKNOWLEDGEMENTS

²² Put your acknowledgements here.

²³

²⁴ And potentially a second round.

²⁵

26 CONTENTS

27	I	INTRODUCTION	1
28	1	INTRODUCTION	3
29	II	THEORETICAL CONTEXT	5
30	2	STANDARD MODEL	7
31	2.1	Particles	7
32	2.2	Interactions	8
33	2.3	Limitations	8
34	3	SUPERSYMMETRY	9
35	3.1	Motivation	9
36	3.2	Structure	9
37	3.3	Phenomenology	9
38	4	LONG-LIVED PARTICLES	11
39	4.1	Mechanisms	11
40	4.1.1	Examples in Supersymmetry	11
41	4.2	Phenomenology	11
42	4.2.1	Disimilarities to Prompt Decays	11
43	4.2.2	Characteristic Signatures	11
44	III	EXPERIMENTAL STRUCTURE AND RECONSTRUCTION	13
45	5	THE LARGE HADRON COLLIDER	15
46	5.1	Injection Chain	15
47	5.2	Design and Parameters	15
48	5.3	Luminosity	15
49	6	THE ATLAS DETECTOR	17
50	6.1	Coordinate System	17
51	6.2	Magnetic Field	17
52	6.3	Inner Detector	17
53	6.3.1	Pixel Detector	17
54	6.3.2	Semiconductor Tracker	17
55	6.3.3	Transition Radiation Tracker	17
56	6.4	Calorimetry	17
57	6.4.1	Electromagnetic Calorimeters	17
58	6.4.2	Hadronic Calorimeters	17
59	6.4.3	Forward Calorimeters	17
60	6.5	Muon Spectrometer	17
61	6.6	Trigger	17
62	6.6.1	Trigger Scheme	17
63	6.6.2	Missing Transverse Energy Triggers	17
64	7	EVENT RECONSTRUCTION	19
65	7.1	Tracks and Vertices	19

66	7.1.1	Track Reconstruction	19
67	7.1.2	Vertex Reconstruction	19
68	7.2	Jets	19
69	7.2.1	Topological Clustering	19
70	7.2.2	Jet Energy Scale	19
71	7.2.3	Jet Energy Scale Uncertainties	19
72	7.2.4	Jet Energy Resolution	19
73	7.3	Electrons	19
74	7.3.1	Electron Identification	19
75	7.4	Muons	19
76	7.4.1	Muon Identification	19
77	7.5	Missing Transverse Energy	19
78	IV	CALORIMETER RESPONSE	21
79	8	RESPONSE MEASUREMENT WITH SINGLE HADRONS	23
80	8.1	Dataset and Simulation	24
81	8.1.1	Data Samples	24
82	8.1.2	Simulated Samples	24
83	8.1.3	Event Selection	24
84	8.2	Inclusive Hadron Response	25
85	8.2.1	E/p Distribution	26
86	8.2.2	Zero Fraction	26
87	8.2.3	Neutral Background Subtraction	28
88	8.2.4	Corrected Response	28
89	8.3	Identified Particle Response	34
90	8.3.1	Decay Reconstruction	34
91	8.3.2	Identified Response	35
92	8.3.3	Additional Species in Simulation	37
93	8.4	Summary	38
94	9	JET ENERGY RESPONSE AND UNCERTAINTY	41
95	9.1	Motivation	41
96	9.2	Uncertainty Estimate	41
97	9.3	Summary	44
98	V	SEARCH FOR LONG-LIVED PARTICLES	47
99	10	LONG-LIVED PARTICLES IN ATLAS	49
100	10.1	Overview and Characteristics	49
101	10.2	Simulation	49
102	11	EVENT SELECTION	51
103	11.1	Trigger	52
104	11.2	Kinematics and Isolation	52
105	11.3	Standard Model Rejection	52
106	11.4	Ionization	52
107	11.4.1	dE/dx Calibration	52
108	11.4.2	Mass Estimation	52
109	12	BACKGROUND ESTIMATION	53

110	12.1	Background Sources	53
111	12.2	Prediction Method	53
112	12.3	Validation and Uncertainty	53
113	13	SYSTEMATIC UNCERTAINTIES AND RESULTS	55
114	13.1	Systematic Uncertainties	55
115	13.2	Final Yields	55
116	14	INTERPRETATION	57
117	14.1	Cross Sectional Limits	57
118	14.2	Mass Limits	57
119	14.3	Context for Long-Lived Searches	57
120	VI	CONCLUSIONS	59
121	15	SUMMARY AND OUTLOOK	61
122	15.1	Summary	61
123	15.2	Outlook	61
124	VII	APPENDIX	63
125	A	INELASTIC CROSS SECTION	65
126	B	APPENDIX TEST	67
127	B.1	Appendix Section Test	67
128	B.1.1	Appendix Subection Test	67
129	B.2	A Table and Listing	67
130	B.3	Some Formulas	68
131		BIBLIOGRAPHY	71

132 LIST OF FIGURES

133	Figure 1	The particle content of the Standard Model (SM).	8
134	Figure 2	An illustration (a) of the E/p variable used throughout this paper. The red energy deposits come from the charged particle targeted for measurement, while the blue energy deposits are from nearby neutral particles and must be subtracted. The same diagram (b) for the neutral-background selection, described in Section 8.2.3.	25
135			
136			
137			
138			
139			
140	Figure 3	The E/p distribution and ratio of simulation to data for isolated tracks with (a) $ \eta < 0.6$ and $1.2 < p/\text{GeV} < 1.8$ and (b) $ \eta < 0.6$ and $2.2 < p/\text{GeV} < 2.8$	26
141			
142			
143	Figure 4	The fraction of tracks as a function (a, b) of momentum, (c, d) of interaction lengths with $E \leq 0$ for tracks with positive (on the left) and negative (on the right) charge.	27
144			
145			
146			
147	Figure 5	$\langle E/p \rangle_{\text{BG}}$ as a function of the track momentum for tracks with (a) $ \eta < 0.6$, (b) $0.6 < \eta < 1.1$, and as a function of the track pseudorapidity for tracks with (c) $1.2 < p/\text{GeV} < 1.8$, (d) $1.8 < p/\text{GeV} < 2.2$	29
148			
149			
150			
151	Figure 6	$\langle E/p \rangle_{\text{COR}}$ as a function of track momentum, for tracks with (a) $ \eta < 0.6$, (b) $0.6 < \eta < 1.1$, (c) $1.8 < \eta < 1.9$, and (d) $1.9 < \eta < 2.3$	30
152			
153			
154	Figure 7	$\langle E/p \rangle_{\text{COR}}$ calculated using LCW-calibrated topological clusters as a function of track momentum for tracks with (a) zero or more associated topological clusters or (b) one or more associated topological clusters.	31
155			
156			
157			
158	Figure 8	Comparison of the $\langle E/p \rangle_{\text{COR}}$ for tracks with (a) less than and (b) greater than 20 hits in the TRT.	32
159			
160	Figure 9	Comparison of the $\langle E/p \rangle_{\text{COR}}$ for (a) positive and (b) negative tracks as a function of track momentum for tracks with $ \eta < 0.6$	32
161			
162			
163	Figure 10	Comparison of the E/p distributions for (a) positive and (b) negative tracks with $0.8 < p/\text{GeV} < 1.2$ and $ \eta < 0.6$, in simulation with the FTFP_BERT and QGSP_BERT physics lists.	33
164			
165			
166			
167	Figure 11	Comparison of the response of the hadronic calorimeter as a function of track momentum (a) at the EM-scale and (b) after the LCW calibration.	33
168			
169			
170	Figure 12	Comparison of the response of the EM calorimeter as a function of track momentum (a) at the EM-scale and (b) with the LCW calibration.	34
171			
172			

173	Figure 13	The reconstructed mass peaks of (a) K_S^0 , (b) Λ , and (c) $\bar{\Lambda}$ candidates.	35
174			
175	Figure 14	The E/p distribution for isolated (a) π^+ , (b) π^- , (c) proton, and (d) anti-proton tracks.	36
176			
177	Figure 15	The fraction of tracks with $E \leq 0$ for identified (a) π^+ and π^- , and (b) proton and anti-proton tracks	36
178			
179	Figure 16	The difference in $\langle E/p \rangle$ between (a) π^+ and π^- (b) p and π^+ , and (c) \bar{p} and π^-	37
180			
181	Figure 17	$\langle E/p \rangle_{\text{COR}}$ as a function of track momentum for (a) π^+ tracks and (b) π^- tracks.	38
182			
183	Figure 18	The ratio of the calorimeter response to single parti- cles of various species to the calorimeter response to π^+ with the physics list FTFP_BERT.	38
184			
185	Figure 19	The spectra of true particles inside anti- k_t , $R = 0.4$ jets with (a) $90 < p_T/\text{GeV} < 100$, (b) $400 < p_T/\text{GeV} <$ 500 , and (c) $1800 < p_T/\text{GeV} < 2300$	42
186			
187	Figure 20	The jet energy scale (JES) uncertainty contributions, as well as the total JES uncertainty, as a function of jet p_T for (a) $ \eta < 0.6$ and (b) $0.6 < \eta < 1.1$	44
188			
189	Figure 21	The JES correlations as a function of jet p_T and $ \eta $ for jets in the central region of the detector.	45
190			
191			
192			
193			

194 LIST OF TABLES

₂₀₀ LISTINGS

₂₀₁ Listing 1	A floating example (<code>listings</code> manual)	68
--------------------------	--	----

202 ACRONYMS

203 SM Standard Model

204 LHC Large Hadron Collider

205 ToT time over threshold

206 LCW local cluster weighted

207 MIP minimally ionizing particle

208 EPJC European Physical Journal C

209 JES jet energy scale

210

PART I

211

INTRODUCTION

212

You can put some informational part preamble text here.

1

213

214 INTRODUCTION

215

PART II

216

THEORETICAL CONTEXT

217

You can put some informational part preamble text here.

2

218

219 STANDARD MODEL

220 The SM of particle physics seeks to explain the symmetries and interactions of
221 all currently discovered fundamental particles. It has been tested by several genera-
222 tions of experiments and has been remarkably successful, no significant de-
223 viations have been found. The SM provides predictions in particle physics for
224 interactions up to the Planck scale (10^{15} - 10^{19} GeV).

225 The theory itself is a quantum field theory grown from an underlying $SU(3) \times$
226 $SU(2) \times U(1)$ that requires the particle content and quantum numbers consist-
227 ent with experimental observations (see Section 2.1). Each postulated symme-
228 try is accompanied by an interaction between particles through gauge invari-
229 ance. These interactions are referred to as the Strong, Weak, and Electromag-
230 netic forces, which are discussed in Section 2.2.

231 Although this model has been very predictive, the theory is incomplete; for
232 example, it is not able to describe gravity or astronomically observed dark matter.
233 These limitations are discussed in more detail in Section 2.3.

234 21 PARTICLES

235 The most familiar matter in the universe is made up of protons, neutrons, and
236 electrons. Protons and neutrons are composite particles, however, and are made
237 up in turn by particles called quarks. Quarks carry both electric charge and color
238 charge, and are bound in color-neutral combinations called baryons. The elec-
239 tron is an example of a lepton, and carries only electric charge. Another type
240 of particle, the neutrino, does not form atomic structures in the same way that
241 quarks and leptons do because it carries no color or electric charge. Collectively,
242 these types of particles are known as fermions, the group of particles with half-
243 integer spin.

244 There are three generations of fermions, although familiar matter is formed
245 predominantly by the first generation. The generations are identical except for
246 their masses, which increase in each generation by convention. In addition, each
247 of these particles is accompanied by an antiparticle, with opposite-sign quantum
248 numbers but the same mass.

249 The fermions comprise what is typically considered matter, but there are
250 additional particles that are mediators of interactions between those fermions.
251 These mediators are known as the gauge bosons, gauge in that their existence
252 is required by gauge invariance (discussed further in Section 2.2) and bosons in
253 that they have integer spin. The boson which mediates the electromagnetic force
254 is the photon, the first boson to be discovered; it has no electric charge, no mass,
255 and a spin of 1. There are three spin-1 mediators of the weak force, the two W
bosons and the Z boson. The W bosons have electric charge of ± 1 and a mass of
256 80.385 ± 0.015 GeV, while the Z boson is neutral and has a mass of $91.1876 \pm$

258 0.0021 GeV. The strong force is mediated by eight particles called gluons, which
 259 are massless and electrically neutral but do carry color charge.

260 The final particle present in the SM is the Higgs boson, which was recently
 261 observed for the first time by experiments at CERN in 2012. It is electrically
 262 neutral, has a mass of 125.7 ± 0.4 GeV, and is the only spin-0 particle yet to be
 263 observed. The Higgs boson is the gauge boson associated with the mechanism
 264 that gives a mass to the W and Z bosons.

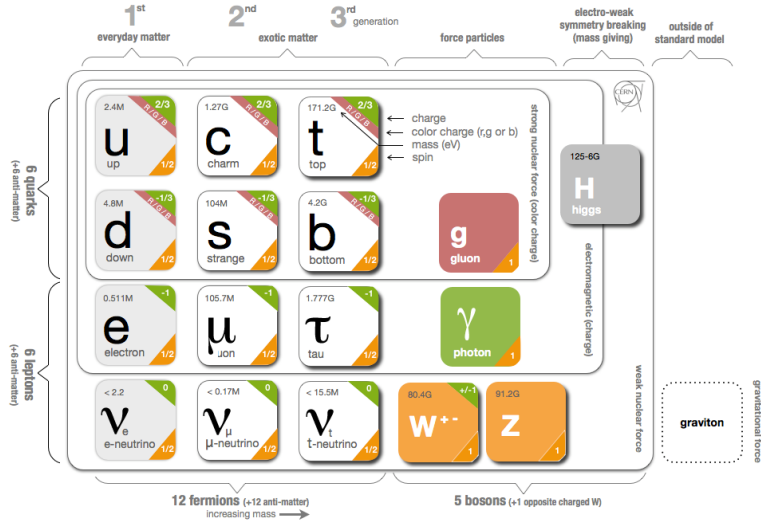


Figure 1: The particle content of the SM.

265 Together these particles form the entire content of the SM, and are summarized
 266 in Figure 1. These are the particles that constitute the observable universe
 267 and all the so-far-observed interactions within it.

268 2.2 INTERACTIONS

269 The interactions predicted and described by the SM are fundamentally tied to the
 270 particles within it, both in that they describe the way those particles can influence
 271 each other and also in that the existence of the interactions requires the existence
 272 of some particles (the gauge bosons).

273 2.3 LIMITATIONS

3

274

275 SUPERSYMMETRY

276 3.1 MOTIVATION

277 3.2 STRUCTURE

278 3.3 PHENOMENOLOGY

4

279

280 LONG-LIVED PARTICLES

281 4.1 MECHANISMS

282 4.1.1 EXAMPLES IN SUPERSYMMETRY

283 4.2 PHENOMENOLOGY

284 4.2.1 DISIMILARITIES TO PROMPT DECAYS

285 4.2.2 CHARACTERISTIC SIGNATURES

286

PART III

287

EXPERIMENTAL STRUCTURE AND RECONSTRUCTION

288

You can put some informational part preamble text here.

5

289

290 THE LARGE HADRON COLLIDER

291 5.1 INJECTION CHAIN

292 5.2 DESIGN AND PARAMETERS

293 5.3 LUMINOSITY

6

294

295 THE ATLAS DETECTOR

296 6.1 COORDINATE SYSTEM

297 6.2 MAGNETIC FIELD

298 6.3 INNER DETECTOR

299 6.3.1 PIXEL DETECTOR

300 6.3.2 SEMICONDUCTOR TRACKER

301 6.3.3 TRANSITION RADIATION TRACKER

302 6.4 CALORIMETRY

303 6.4.1 ELECTROMAGNETIC CALORIMETERS

304 6.4.2 HADRONIC CALORIMETERS

305 6.4.3 FORWARD CALORIMETERS

306 6.5 MUON SPECTROMETER

307 6.6 TRIGGER

308 6.6.1 TRIGGER SCHEME

309 6.6.2 MISSING TRANSVERSE ENERGY TRIGGERS

7

310

311 EVENT RECONSTRUCTION

312 The ATLAS experiment combines measurements in the subdetectors to form a
313 cohesive picture of each physics event.

314 7.1 TRACKS AND VERTICES

315 7.1.1 TRACK RECONSTRUCTION

316 7.1.1.1 NEURAL NETWORK

317 7.1.1.2 PIXEL DE/DX

318 7.1.2 VERTEX RECONSTRUCTION

319 7.2 JETS

320 7.2.1 TOPOLOGICAL CLUSTERING

321 7.2.2 JET ENERGY SCALE

322 7.2.3 JET ENERGY SCALE UNCERTAINTIES

323 7.2.4 JET ENERGY RESOLUTION

324 7.3 ELECTRONS

325 7.3.1 ELECTRON IDENTIFICATION

326 7.4 MUONS

327 7.4.1 MUON IDENTIFICATION

328 7.5 MISSING TRANSVERSE ENERGY

329

PART IV

330

CALORIMETER RESPONSE

331

You can put some informational part preamble text here.

8

332

333 RESPONSE MEASUREMENT WITH SINGLE HADRONS

334 As discussed in Section 7.2, colored particles produced in collisions hadronize
335 into jets of multiple hadrons. One approach to understanding jet physics in the
336 ATLAS calorimetry is to evaluate the calorimeter response to those individual
337 hadrons; measurements of individual hadrons can be used to build up an under-
338 standing of the jets that they form. The redundancy of the momentum provided
339 by the tracking system and the energy provided by the calorimeter provides an
340 opportunity to study calorimeter response using real collisions, as described fur-
341 ther in Section 8.2.

342 Calorimeter response includes a number of physical effects that can be ex-
343 tracted to provide insight into many aspects of jet modeling. First, many charged
344 hadrons interact with the material of the detector prior to reaching the calorime-
345 ters and thus do not deposit any energy. Comparing this effect in data and sim-
346 ulation is a powerful tool in validating the interactions of particles with the ma-
347 terial of the detector and the model of the detector geometry in simulation, see
348 Section 8.2.2. The particles which do reach the calorimeter deposit their energy
349 into individual cells, which are then clustered to measure full energy deposits.
350 Comparing the response in data to simulated hadrons provides a direct evalua-
351 tion of noise in the calorimeters, the showering of hadronic particles, and the
352 energy deposited by particles in matter (Section 8.2.4). These measurements are
353 extended to explore several additional effects, such as the dependence on charge,
354 in Section 8.2.4.1.

355 The above studies all use an inclusive selection of charged particles, which are
356 comprised predominantly of pions, kaons, and (anti)protons. It is also possible
357 to measure the particle types separately to evaluate the simulated interactions of
358 each particle, particularly at low energies where differences between species are
359 very relevant. Pions and (anti)protons can be identified through decays of long-
360 lived particles, in particular Λ , $\bar{\Lambda}$, and K_S^0 , and then used to measure response as
361 described above. This is discussed in detail in Section 8.3.

362 Together, these measurements in data provide a thorough understanding of
363 the way hadrons interact with the ATLAS detector and can be used to build up a
364 description of jets, as seen in Chapter 9. The results in this chapter use data col-
365 lected at 7 and 8 TeV collected in 2010 and 2012, respectively. Both are included
366 as the calorimeter was repaired and recalibrated between those two data-taking
367 periods. Both sets of data are compared to an updated simulation that includes
368 new physics models provided by Geant4 [12] and improvements in the detec-
369 tor description [2, 6]. These results are published in European Physical Journal
370 C (EPJC) [8] and can be compared to a similar measurement performed in 2009
371 and 2010 [5], which used the previous version of the simulation framework [1].

372 8.1 DATASET AND SIMULATION

373 8.1.1 DATA SAMPLES

374 The two datasets used in this chapter are taken from dedicated low-pileup runs
 375 where the fraction of events with multiple interactions was negligible, to facilitate
 376 measurement of isolated hadrons. The 2012 dataset at $\sqrt{s} = 8$ TeV contains
 377 8 million events and corresponds to an integrated luminosity of 0.1 nb^{-1} . The
 378 2010 dataset at $\sqrt{s} = 7$ TeV contains 3 million events and corresponds to an
 379 integrated luminosity of 3.2 nb^{-1} . The latter dataset was also used in the 2010
 380 results [5], but it has since been reanalyzed with an updated detector description
 381 for the material and alignment.

382 8.1.2 SIMULATED SAMPLES

383 The two datasets above are compared to simulated single-, double-, and non-
 384 diffractive events generated with Pythia8 [32] using the A2 configuration of
 385 hadronization [3] and the MSTW 2008 parton-distribution function set [28, 31].
 386 The conditions and energies for each run are matched in the two simulations.

387 To evaluate the interaction of hadrons with detector material, the simulation
 388 uses two different collections of hadronic physics models, called physics lists, in
 389 Geant4 9.4 [30]. The first, QGSP_BERT, combines the Bertini intra-nuclear
 390 cascade [17, 24, 26] below 9.9 GeV, a parametrized proton inelastic model from
 391 9.5 to 25 GeV [21], and a quark-gluon string model above 12 GeV [13, 14, 18, 19,
 392 22]. The second, FTFP_BERT, combines the Bertini intra-nuclear cascade [17, 24,
 393 26] below 5 GeV and the Fritiof model [15, 16, 23, 29] above 4 GeV. In either list,
 394 Geant4 enforces a smooth transition between models where multiple models
 395 overlap.

396 8.1.3 EVENT SELECTION

397 The event selection for this study is minimal, as the only requirement is selecting
 398 good-quality events with an isolated track. Such events are triggered by requiring
 399 at least two hits in the minimum-bias trigger scintillators. After trigger, each
 400 event is required to have exactly one reconstructed vertex, and that vertex is re-
 401 quired to have four or more associated tracks.

402 The particles which enter into the response measurements are first identified
 403 as tracks in the inner detector. The tracks are required to have at least 500 MeV
 404 of transverse momentum. To ensure a reliable momentum measurement, these
 405 tracks are required to have at least one hit in the pixel detector, six hits in the SCT,
 406 and small longitudinal and transverse impact parameters with respect to the pri-
 407 mary vertex [5]. For the majority of the measurements in this chapter, the track is
 408 additionally required to have 20 hits in the TRT, which significantly reduces the
 409 contribution from tracks which undergo nuclear interactions. This requirement
 410 and its effect is discussed in more detail in Section 8.2.4.1. In addition, tracks are
 411 rejected if there is another track which extrapolates to the calorimeter within a

cone of $\Delta R = \sqrt{(\Delta\phi)^2 + (\Delta\eta)^2} < 0.4$. This requirement guarantees that the contamination of energy from nearby charged particles is negligible [5].

8.2 INCLUSIVE HADRON RESPONSE

The calorimeter response is more precisely defined as the ratio of the measured calorimeter energy to the true energy carried by the particle, although this true energy is unknown. For charged particles, however, the inner detector provides a very precise measurement of momentum (with uncertainty less than 1%) that can be used as a proxy for true energy. The ratio of the energy deposited by the charged particle in the calorimeter, E , to its momentum measured in the inner detector p , forms the calorimeter response measure called E/p . Though the distribution of E/p contains a number of physical features, this study focuses on the trends in two aggregated quantities: $\langle E/p \rangle$, the average of E/p within a given subset of particles, and the zero fraction, the fraction of particles with no associated energy in the calorimeter.

The calorimeter energy assigned to a track particle is defined using clusters. The clusters are formed using a 4–2–0 algorithm [9] that begins with seeds requiring at least 4 times the average calorimeter noise. The neighboring cells with at least twice that noise threshold are then added to the cluster, and all bounding cells are then added with no requirement. This algorithm minimizes noise contributions through its seeding process, and including the additional layers improves the energy resolution [33]. The clusters are associated to a given track if they fall within a cone of $\Delta R = 0.2$ of the extrapolated position of the track, which includes about 90% of the energy on average [5]. This construction is illustrated in Figure 2.

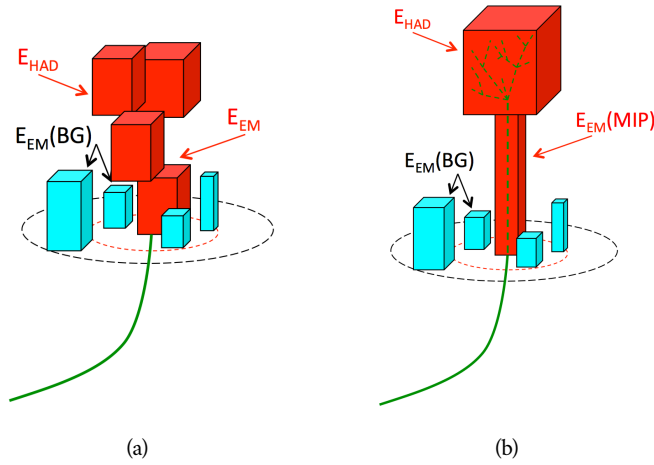
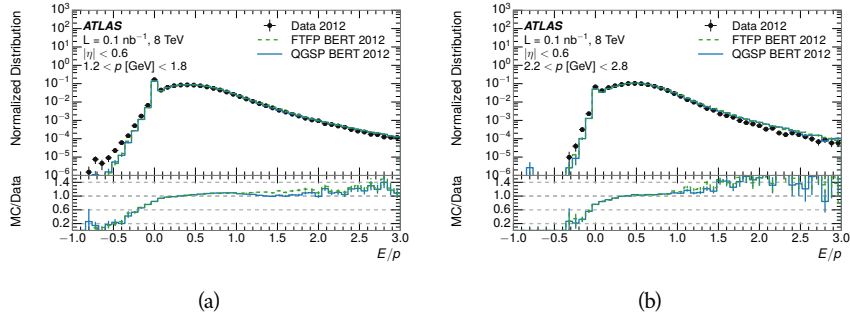


Figure 2: An illustration (a) of the E/p variable used throughout this paper. The red energy deposits come from the charged particle targeted for measurement, while the blue energy deposits are from nearby neutral particles and must be subtracted. The same diagram (b) for the neutral-background selection, described in Section 8.2.3.

436 8.2.1 E/P DISTRIBUTION

437 The E/p distributions measured in both data and simulation are shown in Figure 3 for two example bins of track momentum and for tracks in the central
 438 region of the detector. These distributions show several important features of
 439 the E/p observable. The large content in the bin at $E = 0$ comes from tracks that
 440 have no associated cluster, which occurs due to interactions with detector mate-
 441 rial prior to reaching the calorimeter or the energy deposit being insufficiently
 442 large to generate a seed, and are discussed in Section 8.2.2. The small negative
 443 tail comes from similar tracks that do not deposit any energy in the calorime-
 444 ter but are randomly associated to a noise cluster. The long positive tail above
 445 1.0 comes from the contribution of neutral particles. Nearby neutral particles
 446 deposit (sometimes large) additional energy in the calorimeter but do not pro-
 447 duce tracks in the inner detector, so they cannot be rejected by the track isol-
 448 ation requirement. Additionally the peak and mean of the distribution falls below
 449 1.0 because of the loss of energy not found within the cone as well as the non-
 450 compensation of the calorimeter.
 451

452 The data and simulation share the same features, but the high and low tails
 453 are significantly different. The simulated events tend to overestimate the contri-
 454 bution of neutral particles to the long tail, an effect which can be isolated and
 455 removed as discussed in Section 8.2.3. Additionally, the simulated clusters have
 456 less noise on average, although this is a small effect on the overall response.



457 Figure 3: The E/p distribution and ratio of simulation to data for isolated tracks with
 458 (a) $|\eta| < 0.6$ and $1.2 < p/\text{GeV} < 1.8$ and (b) $|\eta| < 0.6$ and $2.2 < p/\text{GeV} < 2.8$.

457 8.2.2 ZERO FRACTION

458 The fraction of particles with no associated clusters, or similarly those with $E \leq$
 459 0, reflects the modeling of both the detector geometry and hadronic interactions.
 460 The zero fraction is expected to rise as the amount of material a particle traverses
 461 increases, while it is expected to decrease as the particle energy increases. This
 462 dependence can be seen in Figure 4, where the zero fraction in data and simula-
 463 tion is shown as a function of momentum and the amount of material measured
 464 in interaction lengths. The trends are similar between the 2010 and 2012 mea-
 465 surements. The zero fraction decreases with energy as expected. The amount of

material in the detector increases with η , which provides a distribution of interaction lengths. As the data and simulation have significant disagreement in the zero fraction over a number of interaction lengths, the difference must be primarily from the modeling of hadronic interactions with detector material and not just the detector geometry.

There is also a noticeable difference between positive and negative tracks at low momentum, which reflects the difference in response between protons and antiprotons. Antiprotons have significant model differences in the two physics lists, QGSP_BERT and FTFP_BERT, and this is evident in the lowest momentum bin of the data to simulation ratio. This difference is explored further in Section 8.3.

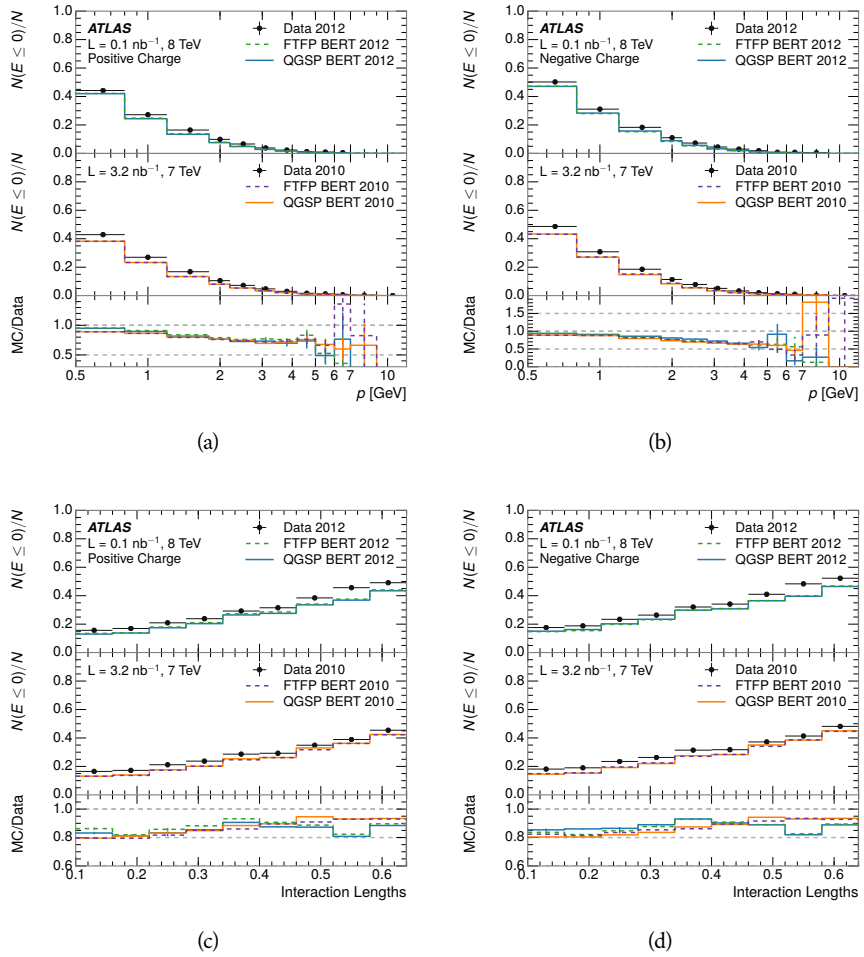


Figure 4: The fraction of tracks as a function (a, b) of momentum, (c, d) of interaction lengths with $E \leq 0$ for tracks with positive (on the left) and negative (on the right) charge.

477 8.2.3 NEUTRAL BACKGROUND SUBTRACTION

478 The isolation requirement on hadrons is only effective in remove energy contri-
 479 bution from nearby charged particles. Nearby neutral particles, predominantly
 480 photons from π^0 decays, also add their energy to the calorimeter clusters, but
 481 mostly in the electromagnetic calorimeter. It is possible to measure this contri-
 482 bution, on average, using late-showering hadrons that minimally ionize in the
 483 electromagnetic calorimeter. Such particles are selected by requiring that they
 484 deposit less than 1.1 GeV in the EM calorimeter within a cone of $\Delta R < 0.1$
 485 around the track. To ensure that these particles are well measured, they are addi-
 486 tionally required to deposit between 40% and 90% of their energy in the hadronic
 487 calorimeter within the same cone.

488 These particles provide a clean sample to measure the nearby neutral back-
 489 ground because they do not deposit energy in the area immediately surrounding
 490 them in the EM calorimeter, as shown in Figure 2. So, the energy deposits in the
 491 region $0.1 < \Delta R < 0.2$ can be attributed to neutral particles alone. To estimate
 492 the contribution to the whole cone considered for the response measurement,
 493 that energy is scaled by a geometric factor of 4/3. This quantity, $\langle E/p \rangle_{\text{BG}}$, mea-
 494 sured in aggregate over a number of particles, gives the contribution to $\langle E/p \rangle$
 495 from neutral particles in the EM calorimeter. Similar techniques were used in
 496 the individual layers of the hadronic calorimeters to show that the background
 497 from neutrals is negligible in those layers [5].

498 The distribution of this background estimate is shown in Figure 5. Although
 499 the simulation captures the overall trend, it significantly overestimates the neu-
 500 tral contribution for tracks with momentum between 2 and 8 GeV. This effect
 501 was also seen in the tails of the E/p distributions in Figure 3. This difference is
 502 likely due to the modeling of coherent neutral particle radiation in Pythia8, as
 503 the discrepancy does not depend on η and thus is unlikely to be a mismodeling
 504 of the detector. This difference can be subtracted to form a corrected average
 505 E/p , as in Section 8.2.4.

506 8.2.4 CORRECTED RESPONSE

507 Figure 6 shows $\langle E/p \rangle_{\text{COR}}$ as a function of momentum for several bins of pseu-
 508 dorapidity. This corrected $\langle E/p \rangle_{\text{COR}} \equiv \langle E/p \rangle - \langle E/p \rangle_{\text{BG}}$ measures the average
 509 calorimeter response without the contamination of neutral particles. It is the
 510 most direct measurement of calorimeter response in that it is the energy mea-
 511 sured for fully isolated hadrons. The correction is performed separately in data
 512 and simulation, so that the mismodeling of the neutral background in simulation
 513 is removed from the comparison of response. The simulation overestimates the
 514 response at low momentum by about 5%, an effect that can be mostly attributed
 515 to the underestimation of the zero fraction mentioned previously.

516 The response measurement above used topological clustering at the EM scale,
 517 that is clusters were formed to measure energy but no corrections were applied
 518 to correct for expected effects like energy lost outside of the cluster or in unin-
 519 strumented material. It is also interesting to measure $\langle E/p \rangle_{\text{COR}}$ using local clus-

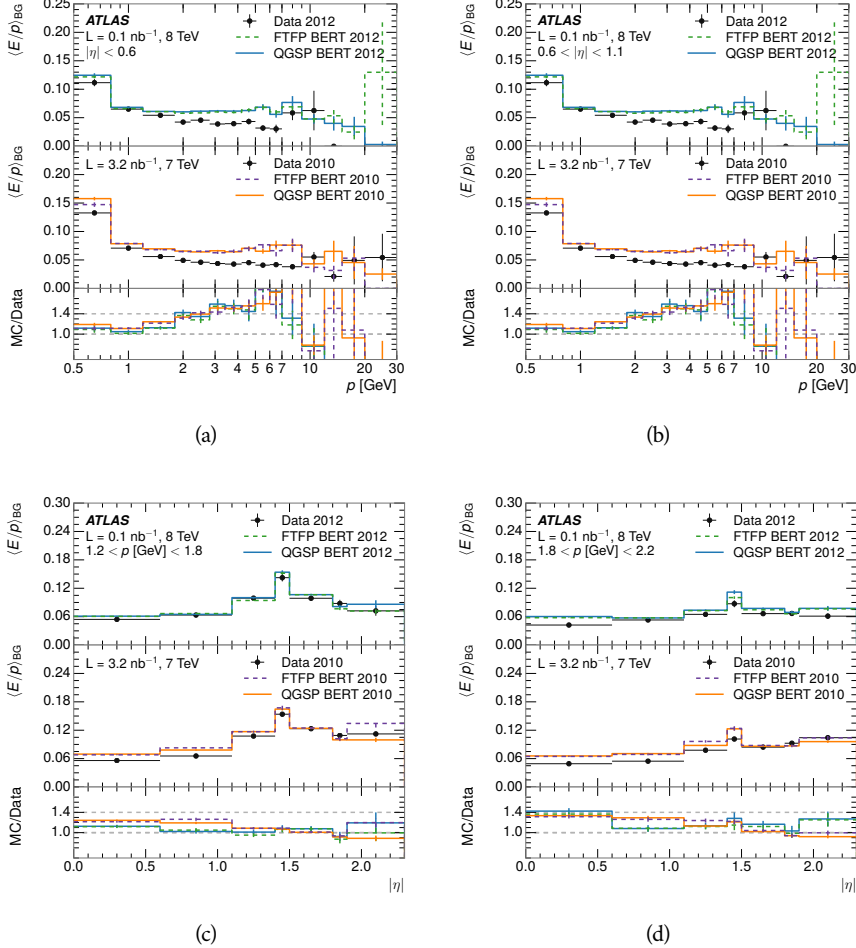


Figure 5: $\langle E/p \rangle_{BG}$ as a function of the track momentum for tracks with (a) $|\eta| < 0.6$, (b) $0.6 < |\eta| < 1.1$, and as a function of the track pseudorapidity for tracks with (c) $1.2 < p/\text{GeV} < 1.8$, (d) $1.8 < p/\text{GeV} < 2.2$.

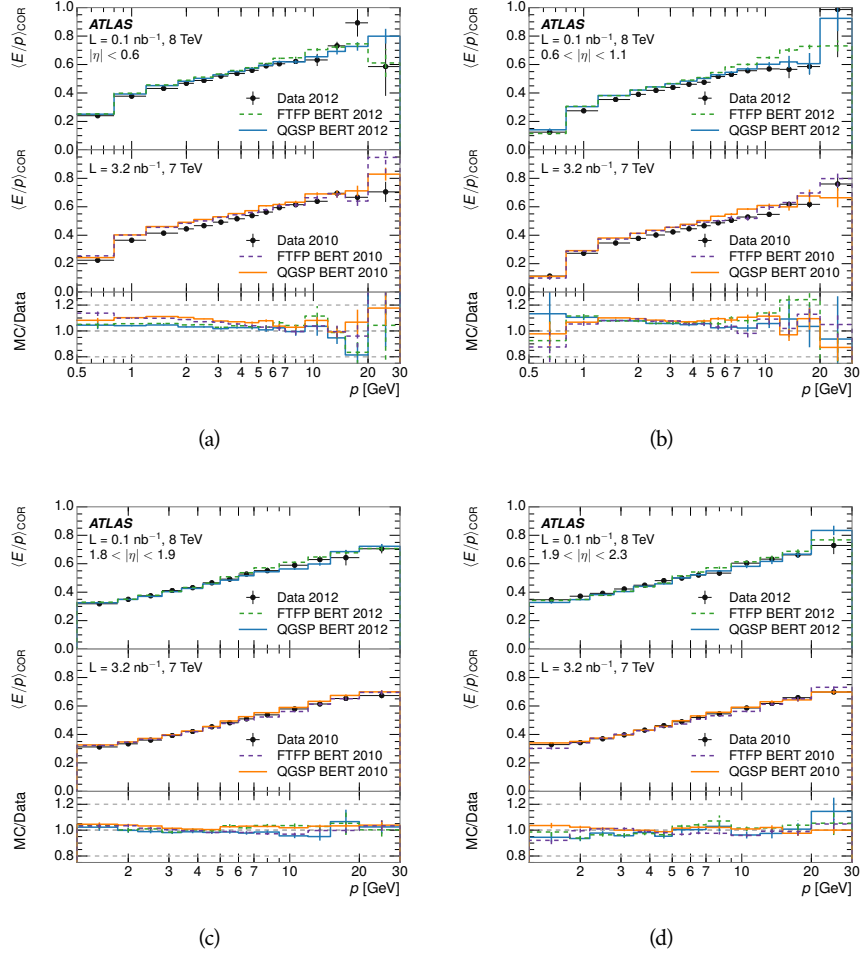


Figure 6: $\langle E/p \rangle_{\text{COR}}$ as a function of track momentum, for tracks with (a) $|\eta| < 0.6$, (b) $0.6 < |\eta| < 1.1$, (c) $1.8 < |\eta| < 1.9$, and (d) $1.9 < |\eta| < 2.3$.

520 ter weighted (LCW) energies, which accounts for those effects by calibrating the
 521 energy based on the properties of the cluster such as energy density and depth
 522 in the calorimeter. Figure 7 shows these distributions for tracks with zero or
 523 more clusters and separately for tracks with one or more clusters. The calibra-
 524 tion moves $\langle E/p \rangle_{\text{COR}}$ significantly closer to 1.0, which is the purpose of the cali-
 525 bration. The agreement between data and simulation improves noticeably when
 526 at least one cluster is required, as this removes the contribution from the mis-
 527 modeling of the zero fraction.

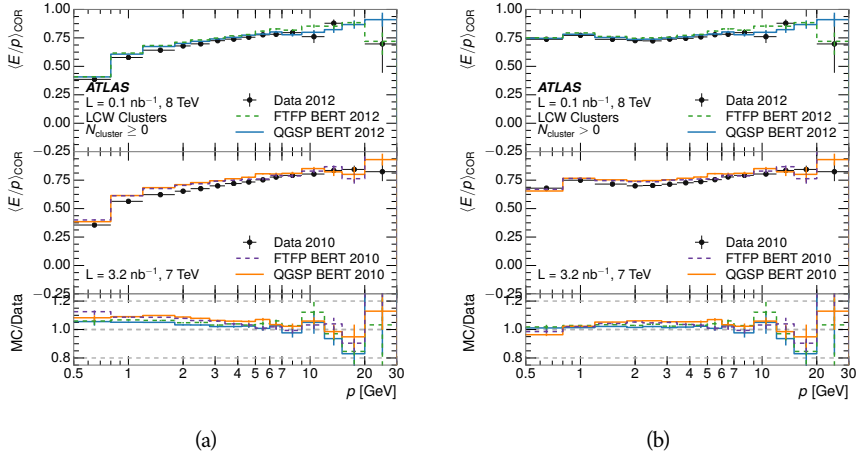


Figure 7: $\langle E/p \rangle_{\text{COR}}$ calculated using LCW-calibrated topological clusters as a function of track momentum for tracks with (a) zero or more associated topological clusters or (b) one or more associated topological clusters.

528 8.2.4.1 ADDITIONAL STUDIES

529 As has been seen in several previous measurements, the simulation does not
 530 correctly model the chance of a low momentum hadron to reach the calorime-
 531 ter. Because of the consistent discrepancy across pseudorapidity and interaction
 532 lengths, this seems to be best explained by incomplete understanding of hadronic
 533 interactions with the detector. For example, a hadron that scatters off of a nu-
 534 cleus in the inner detector can be deflected through a significant angle and not
 535 reach the expected location in the calorimeter. In addition, these interactions can
 536 produce secondary particles that are difficult to model.

537 The requirement on the number of hits in the TRT reduces these effects by
 538 preferentially selecting tracks that do not undergo nuclear interactions. It is in-
 539 teresting to check how well the simulation models tracks with low numbers of
 540 TRT hits, where the nuclear interactions are much more likely. Figure 8 com-
 541 pares the distributions with $N_{\text{TRT}} < 20$ to $N_{\text{TRT}} > 20$ for real and simulated
 542 particles. As expected, the tracks with fewer hits are poorly modeled in the sim-
 543 ulation as $\langle E/p \rangle_{\text{COR}}$ differs by as much as 25% at low momentum.

544 Another interesting aspect of the simulation is the description of antiprotons
 545 at low momentum, where QGSP_BERT and FTFP_BERT have significant differ-
 546 ences. This can be seen to have an effect in the inclusive response measurement

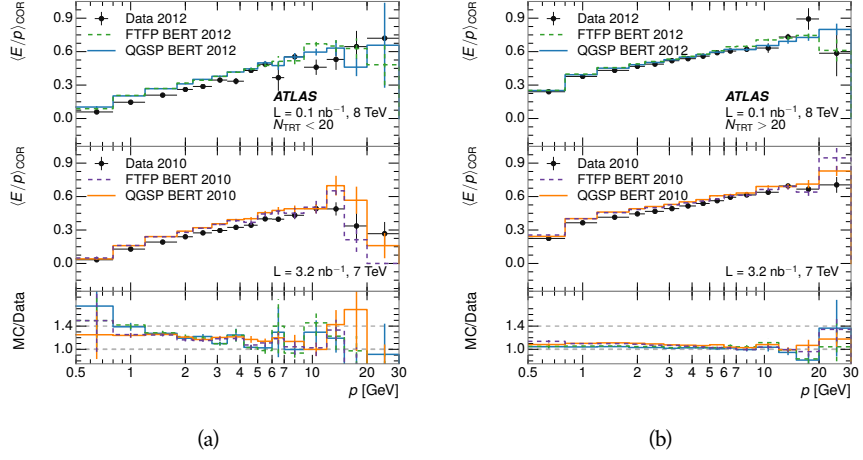


Figure 8: Comparison of the $\langle E/p \rangle_{\text{COR}}$ for tracks with (a) less than and (b) greater than 20 hits in the TRT.

when separated into positive and negative charge. The $\langle E/p \rangle_{\text{COR}}$ distributions for positive and negative particles are shown in Figure 9, where a small difference between QGSP_BERT and FTFP_BERT can be seen in the distribution for negative tracks. This is demonstrated more clearly in Figure 10, which shows the E/p distribution in the two simulations separated by charge. There is a clear difference around $E/p > 1.0$, which can be explained by the additional energy deposited by the annihilation of the antiproton in the calorimeter that is modeled well only in FTFP_BERT. This is also explored with data using identified antiprotons in Section 8.3.

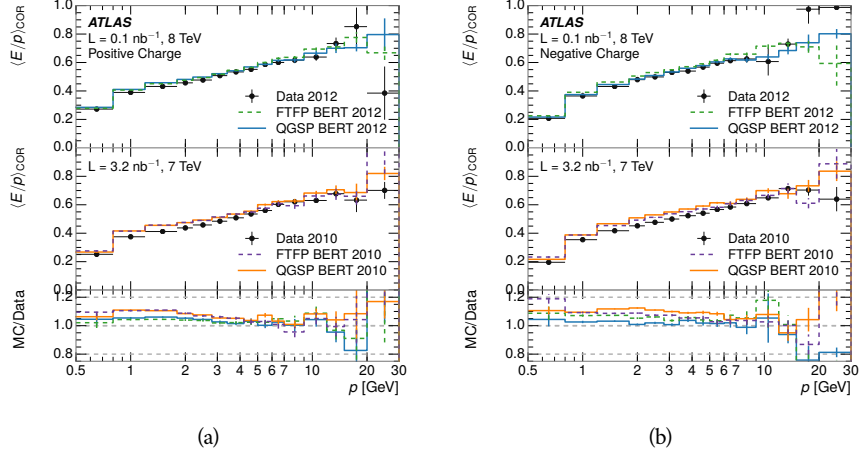


Figure 9: Comparison of the $\langle E/p \rangle_{\text{COR}}$ for (a) positive and (b) negative tracks as a function of track momentum for tracks with $|\eta| < 0.6$.

The $\langle E/p \rangle$ results in previous sections have considered the electromagnetic and hadronic calorimeters together as a single energy measurement, to emphasize the total energy deposited for a given particle. However, the deposits in each

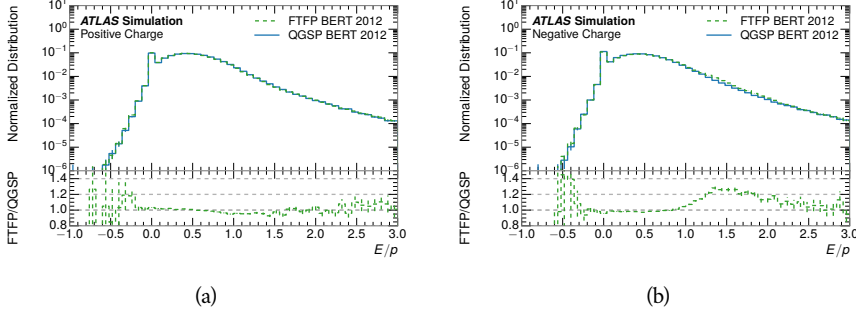


Figure 10: Comparison of the E/p distributions for (a) positive and (b) negative tracks with $0.8 < p/\text{GeV} < 1.2$ and $|\eta| < 0.6$, in simulation with the FTFP_BERT and QGSP_BERT physics lists.

559 calorimeter are available separately and $\langle E/p \rangle$ can be constructed for each layer.
 560 As the layers are composed of different materials and are modeled separately in
 561 the detector geometry, confirmation that the simulation matches the data well
 562 in each layer adds confidence in both the description of hadronic interactions
 563 with the two different materials and also the geometric description of each.

564 The technique discussed in Section 8.2.3 for selecting minimally ionizing par-
 565 ticle (**MIP**)s in the electromagnetic calorimeter is also useful in studying deposits
 566 in the hadronic calorimeter. Those **MIP**s deposit almost all of their energy ex-
 567 clusively in the hadronic calorimeter. Figure 11 shows $\langle E/p \rangle_{\text{RAW}}^{\text{Had}}$, where RAW
 568 indicates that no correction has been applied for neutral backgrounds and Had
 569 indicates that only clusters for the hadronic calorimeter are included. The RAW
 570 and COR versions of $\langle E/p \rangle$ in this case are the same, as the neutral background
 571 is negligible in that calorimeter layer. The distributions are shown both for the
 572 original EM scale calibration and after LCW calibration. The data and simulation
 573 agree very well in this comparison, except in the lowest momentum bin which
 574 has 5% discrepancy that has already been seen in similar measurements.

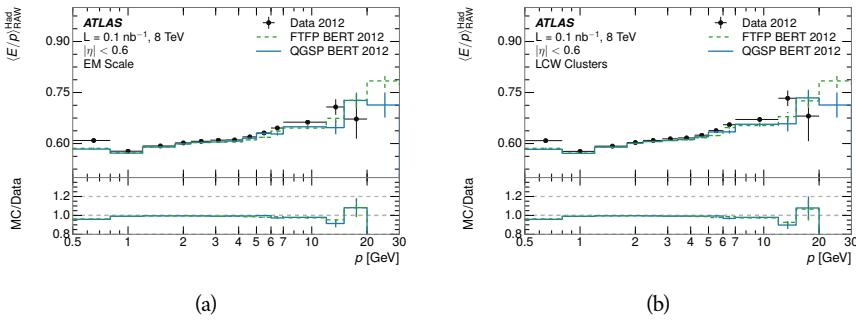


Figure 11: Comparison of the response of the hadronic calorimeter as a function of track momentum (a) at the EM-scale and (b) after the LCW calibration.

575 A similar comparison can be made in the electromagnetic calorimeter by se-
 576 lecting particles which have no associated energy in the hadronic calorimeter.
 577 These results are measured in terms of $\langle E/p \rangle_{\text{COR}}^{\text{EM}}$, where EM designates that

578 only clusters in the electromagnetic calorimeter are included and COR designates that the neutral background is subtracted as the neutral background is
 579 present in this case. Figure 12 shows the analogous comparisons to Figure 11 in
 580 the electromagnetic calorimeter. In this case the disagreement between data and
 581 simulation is more pronounced, with discrepancies as high as 5% over a larger
 582 range of momenta. This level of discrepancy indicates that the description of the
 583 electromagnetic calorimeter is actually the dominant source of discrepancy in
 584 the combined distributions in Section 8.2.4.
 585

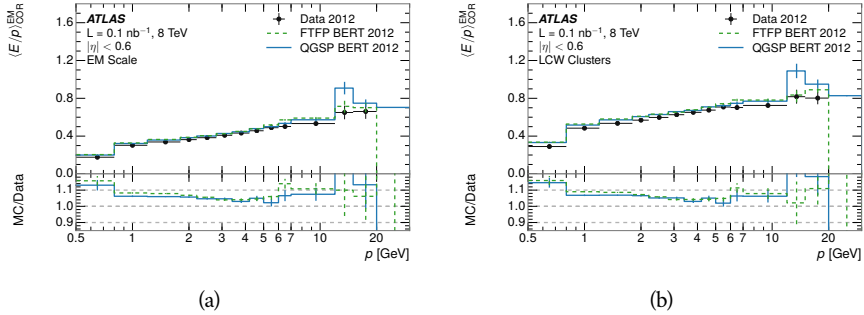


Figure 12: Comparison of the response of the EM calorimeter as a function of track momentum (a) at the EM-scale and (b) with the LCW calibration.

586 **NOTE: There are more studies that I skipped for brevity that could be**
 587 **included if interesting. E/p at different cluster threshold settings, E/p with**
 588 **pileup, E/p with cells. I also left out a lot of eta bins that appear in the paper**
 589 **so that this section didn't turn into 20 pages of plots.**

590 8.3 IDENTIFIED PARTICLE RESPONSE

591 The inclusive response measurement for hadrons can be augmented by measuring
 592 the response for specific particle species. The simulation models each parti-
 593 cle type separately, and understanding the properties of each is important in con-
 594 straining the uncertainty on jets. In order to select and measure specific hadrons,
 595 this section relies on the displaced decays of long-lived particles. Such decays can
 596 be identified by reconstructing secondary vertices with a requirement on mass.
 597 In particular, Λ , $\bar{\Lambda}$, and K_S^0 can be used to select a pure sample of protons, an-
 598 tiprotons, and pions, respectively.

599 8.3.1 DECAY RECONSTRUCTION

600 The measurement of response for identified particles uses the same selection
 601 as for inclusive particles (Section 8.1.3) with a few additions. Each event used
 602 is required to have at least one secondary vertex, and the tracks are required
 603 to match to that vertex rather than the primary vertex. Pions are selected from
 604 decays of $K_S^0 \rightarrow \pi^+ \pi^-$, which is the dominant decay for K_S^0 to charged particles.
 605 Protons are selected from decays of $\Lambda \rightarrow \pi^- p$ and antiprotons from $\bar{\Lambda} \rightarrow \pi^+ \bar{p}$,

which are similarly the dominant decays of Λ and $\bar{\Lambda}$ to charged particles. The species of parent hadron in these decays is determined by reconstructing the mass of the tracks associated to the secondary vertex. The sign of the higher momentum decay particle can distinguish between Λ and $\bar{\Lambda}$, which of course have the same mass, as the proton or antiproton is kinematically favored to have higher momentum. Examples of the reconstructed masses used to select these decays are shown in Figure 13.

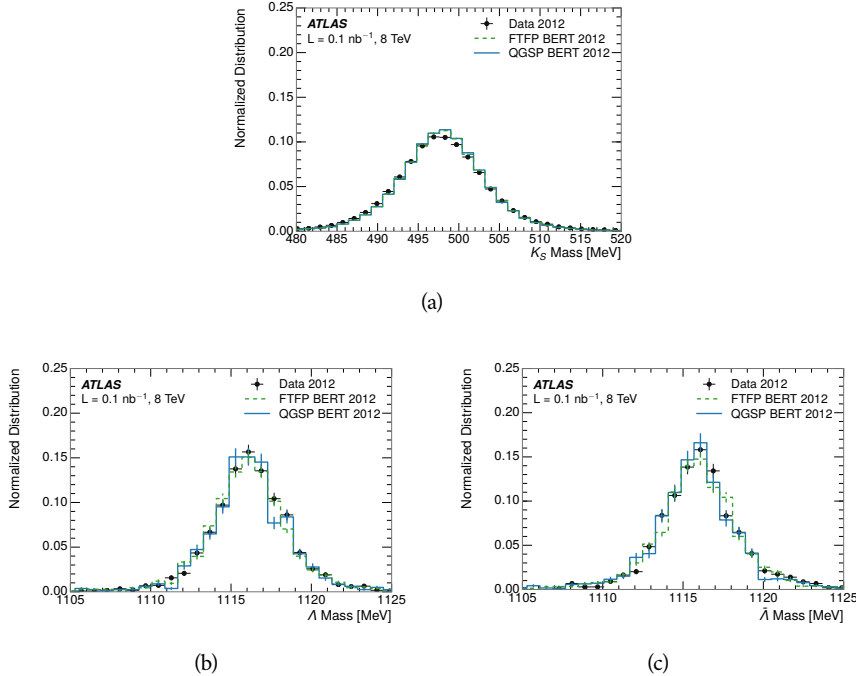


Figure 13: The reconstructed mass peaks of (a) K_S^0 , (b) Λ , and (c) $\bar{\Lambda}$ candidates.

The dominant backgrounds for the identified particle decays are nuclear interactions and combinatoric sources. These are suppressed by the kinematic requirements on the tracks as well as an additional veto which removes candidates that are consistent with both a Λ or $\bar{\Lambda}$ and a K_S^0 hypothesis, which is possible because of the different assumptions on particle mass in each case [5]. After these requirements, the backgrounds are found to be negligible compared to the statistical errors on these measurements.

8.3.2 IDENTIFIED RESPONSE

With these techniques the E/p distributions are extracted in data and simulation for each particle species and shown in Figure 14. These distributions are shown for a particular bin of E_a ($2.2 < E_a/\text{GeV} < 2.8$), rather than p . E_a is the energy available to be deposited in the calorimeter: for pions $E_a = \sqrt{p^2 + m^2}$, for protons $E_a = \sqrt{p^2 + m^2} - m$, and for antiprotons $E_a = \sqrt{p^2 + m^2} + m$. The features of the E/p distributions are similar to the inclusive case. There is a small negative tail from noise and a large fraction of tracks with zero energy from particles which do not reach the calorimeter. The long positive tail is noticeably more

629 pronounced for antiprotons because of the additional energy generated by the
 630 annihilation in addition to the neutral background.

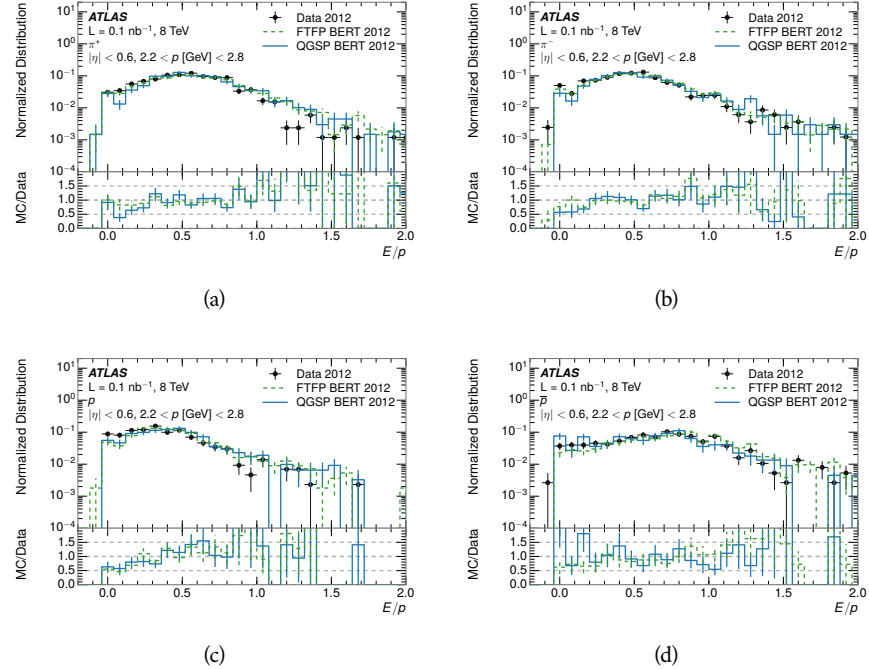


Figure 14: The E/p distribution for isolated (a) π^+ , (b) π^- , (c) proton, and (d) anti-proton tracks.

631 The zero fraction is further explored in Figure 15 for pions and protons in
 632 data and simulation. The simulation consistently underestimates the zero frac-
 633 tion independent of particle species, which implies that this discrepancy is not
 634 caused by the model of a particular species but rather a feature common to all.

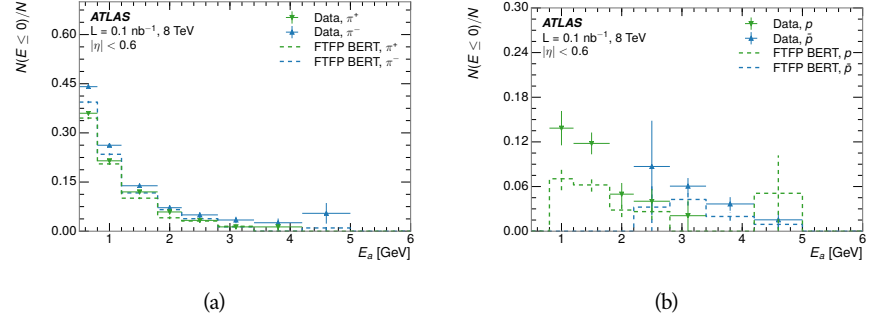


Figure 15: The fraction of tracks with $E \leq 0$ for identified (a) π^+ and π^- , and (b) proton and anti-proton tracks

635 It is also interesting to compare the response between the different particle
 636 species. One approach to do this is to measure the difference in $\langle E/p \rangle$ between
 637 two types, which has the advantage of removing the neutral background. These
 638 differences are shown in various combinations in Figure 16. The response for

639 π^+ is greater on average than the response to π^- because of a charge-exchange
 640 effect which causes the production of additional neutral pions in the showers of
 641 π^+ [20]. The response for π^+ is also greater on average than the response to p ,
 642 because a large fraction of the energy of π^+ hadrons is converted to an electro-
 643 magnetic shower [11, 25]. However, the \bar{p} response is significantly higher than
 644 the response to π^- because of the annihilation of the antiproton. FTFP_BERT
 645 does a better job of modeling this effect than QGSP_BERT because of their differ-
 646 ent descriptions of \bar{p} interactions with material.

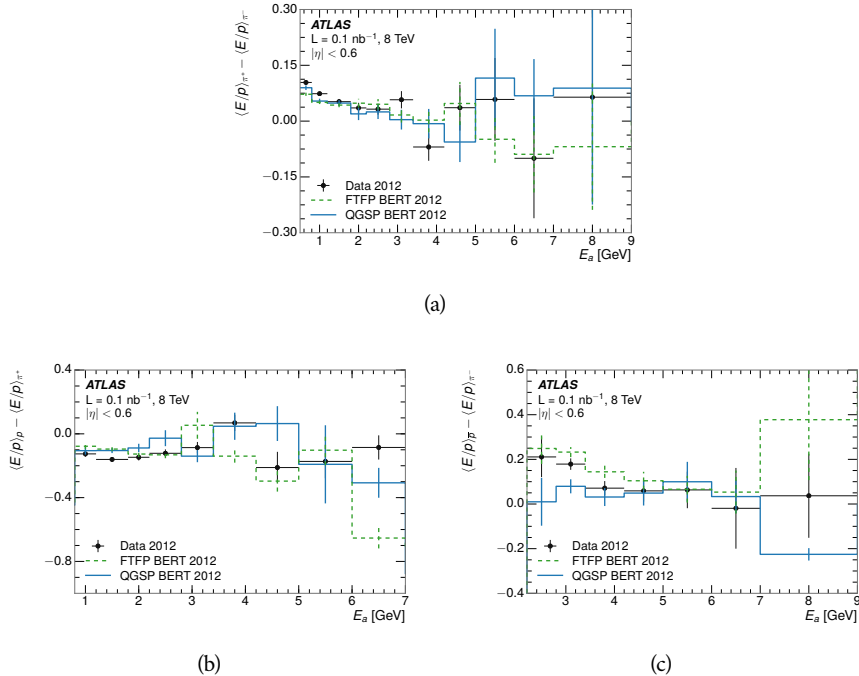


Figure 16: The difference in $\langle E/p \rangle$ between (a) π^+ and π^- (b) p and π^+ , and (c) \bar{p} and π^- .

647 It is also possible to remove the neutral background from these response dis-
 648 tributions using the same technique as in Section 8.2.3. The technique is largely
 649 independent of the particle species and so can be directly applied to $\langle E/p \rangle$ for
 650 pions. The $\langle E/p \rangle_{\text{COR}}$ distributions for pions are shown in Figure 17, which are
 651 very similar to the inclusive results. The inclusive hadrons are comprised mostly
 652 of pions, so this similarity is not surprising. It is also possible to see the small
 653 differences between π^+ and π^- response here, where $\langle E/p \rangle_{\text{COR}}$ is higher on av-
 654 erage for π^+ . The agreement between data and simulation is significantly worse
 655 for the π^- distributions than for the π^+ , with a discrepancy greater than 10%
 656 below 2-3 GeV.

657 8.3.3 ADDITIONAL SPECIES IN SIMULATION

658 The techniques above provide a method to measure the response separately for
 659 only pions and protons. However the hadrons which forms jets include a num-
 660 ber of additional species such as kaons and neutrons. The charged kaons are

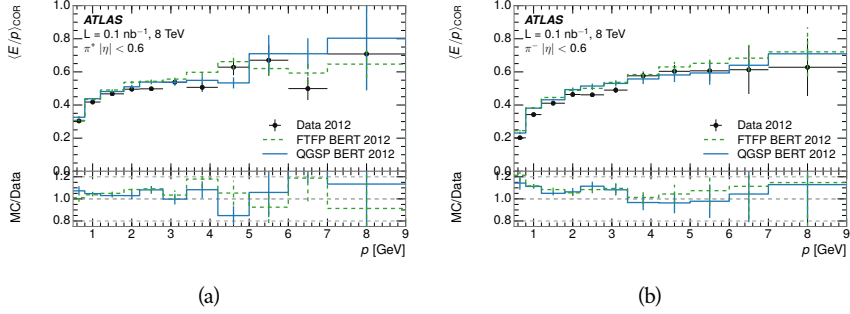


Figure 17: $\langle E/p \rangle_{\text{COR}}$ as a function of track momentum for (a) π^+ tracks and (b) π^- tracks.

an important component of the inclusive charged hadron distribution, which is comprised of roughly 60-70% pions, 15-20% kaons, and 5-15% protons. These are difficult to measure in data at the ATLAS detector, although a template subtraction technique has been proposed which may be effective with larger sample sizes [8]. The simulation of these particles includes noticeable differences in response at low energies, which are shown in Figure 18 for FTFP_BERT. The significant differences in response between low energy protons and antiprotons are accounted for above in the definitions of E_a .

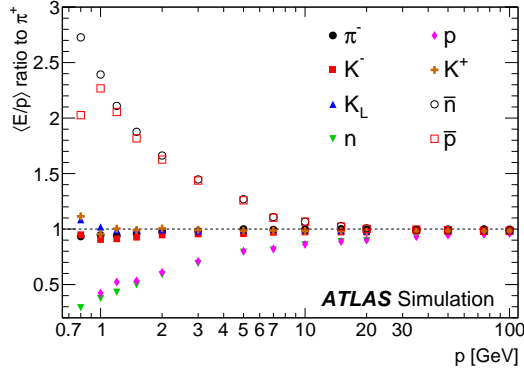


Figure 18: The ratio of the calorimeter response to single particles of various species to the calorimeter response to π^+ with the physics list FTFP_BERT.

8.4 SUMMARY

These various measurements of calorimeter response shown above for data and simulation illuminate the accuracy of the simulation of hadronic interactions at the ATLAS detector. The results were done using 2010 and 2012 data at 7 and 8 TeV, but reflect the most current understanding of the detector alignment and geometry. A number of measurements focusing on a comparison between protons and antiprotons suggest that FTFP_BERT models those interaction more accurately than QGSP_BERT. These measurements, among others, were the moti-

677 vation to switch the default Geant4 simulation from FTFP_BERT to QGSP_BERT
678 for all ATLAS samples.

679 Even with these updates, there are a number of small, approximately 5%, dis-
680 crepancies in response between the data and simulation at low energies. At higher
681 energies the simulation of hadronic interactions is very consistent with data.
682 Chapter 9 discusses how to use these observed differences to constrain the jet
683 energy scale and its associated uncertainties.

684

685 JET ENERGY RESPONSE AND UNCERTAINTY

686 9.1 MOTIVATION

687 As jets form a major component of many physics analyses at ATLAS, it is cru-
 688 cial to carefully calibrate the measurement of jet energies and to derive an un-
 689 certainty on that measurement. These uncertainties have often been the domi-
 690 nant systematic uncertainty in high-energy analyses at the Large Hadron Col-
 691 linder ([LHC](#)). Dijet and multijet balance techniques provide a method to constrain
 692 the [JES](#) and its uncertainty in data, and provide the default values used for ATLAS
 693 jet measurements at most energies [7]. These techniques are limited by their re-
 694 liance on measuring jets in data, so they are statistically limited in estimating
 695 the jet energy scale at the highest jet energies. This chapter presents another
 696 method for estimating the jet energy scale and its uncertainty which builds up a
 697 jet from its components and thus can be naturally extended to high jet momen-
 698 tum. Throughout this chapter the jets studied are simulated using [Pythia8](#) with
 699 the CT10 parton distribution set [27] and the AU2 tune [3], and corrections are
 700 taken from the studies including data and simulation in Chapter 8.

701 As described in Section 7.2, jets are formed from topological clusters of energy
 702 in the calorimeters using the anti- k_t algorithm. These clusters originate from a
 703 diverse spectrum of particles, in terms of both species and momentum, leading to
 704 significantly varied jet properties and response between jets of similar produced
 705 momentum. Figure 19 shows the simulated distribution of particles within jets
 706 at a few examples energies. The E/p measurements provide a thorough under-
 707 standing of the dominant particle content of jets, the charged hadrons.

708 9.2 UNCERTAINTY ESTIMATE

709 Simulated jets are not necessarily expected to correctly model the energy de-
 710 posits in the calorimeters, because of the various discrepancies discussed in Chap-
 711 ter 8. To evaluate a jet energy response, the simulated jet energies are compared
 712 to a corrected jet built up at the particle level. Each cluster in a jet is associated
 713 to the truth particle which deposited it, and the energy in that cluster is then
 714 corrected for a number of effects based on measurements in data. The primary
 715 corrections come from the single hadron response measurements in addition to
 716 response measured using the combined test beam which covers higher momen-
 717 tum particles [10]. These corrections include both a shift (Δ), in order to make the
 718 simulation match the average response in data, and an uncertainty (σ) associated
 719 with the ability to constrain the difference between data and simulation. Some of
 720 the dominant sources of uncertainty are itemized in Table ?? with typical values,
 721 and the full list considered is described in detail in the associated paper [8]. These

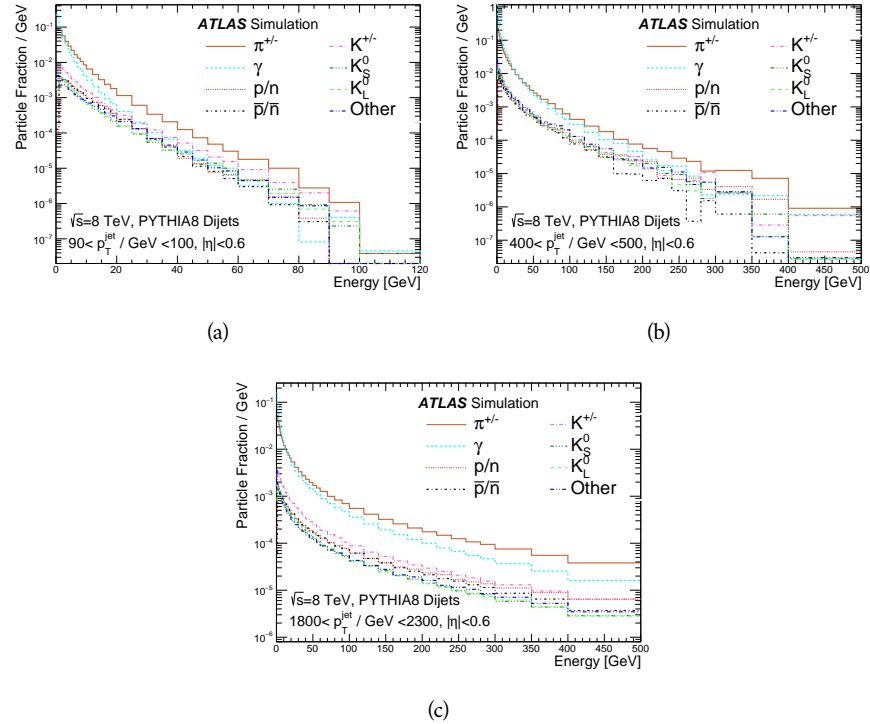


Figure 19: The spectra of true particles inside anti- k_t , $R = 0.4$ jets with (a) $90 < p_T/\text{GeV} < 100$, (b) $400 < p_T/\text{GeV} < 500$, and (c) $1800 < p_T/\text{GeV} < 2300$.

uncertainties cover differences between the data and simulation in the modeling of calorimeter response to a given particle. No uncertainties are added for the difference between particle composition of jets in data and simulation.

From these terms, the jet energy scale and uncertainty is built up from individual energy deposits in simulation. Each uncertainty term is treated independently, and are taken to be gaussian distributed. The resulting scale and uncertainty is shown in Figure 20, where the mean response is measured relative to the calibrated energy reported by simulation. The dominant uncertainties come from the statistical uncertainties on the E/p measurements at lower energies and the additional uncertainty for out of range measurements at higher energies. The total uncertainty from this method at intermediate jet energies is comparable to other simulation-based methods [4] and is about twice as large as in-situ methods using data [7]. This method is the only one which provides an estimation above 1.8 TeV, however, and so is still a crucial technique in analyses that search for very energetic jets.

These techniques can also be used to measure the correlation between bins of average reconstructed jet momentum across a range of p_T and $|\eta|$, where correlations are expected because of a similarity in particle composition at similar energies. Figure 21 shows these correlations, where the uncertainties on jets in neighboring bins are typically between 30% and 60% correlated. The uncertainty on all jets becomes significantly correlated at high energies and larger pseudorapidities, when the uncertainty becomes dominated by the single term reflecting out of range particles.

Abbrev.	Description	Δ (%)	σ (%)
In situ E/p	The comparison of $\langle E/p \rangle_{\text{COR}}$ as described in Chapter 8 with statistical uncertainties from 500 MeV to 20 GeV.	0-3	1-5
CTB	The main $\langle E/p \rangle$ comparison uncertainties, binned in p and $ \eta $, as derived from the combined test beam results, from 20 to 350 GeV [10].	0-3	1-5
E/p Zero Fraction	The difference in the zero-fraction between data and MC simulation from 500 MeV to 20 GeV.	5-25	1-5
E/p Threshold	The uncertainty in the EM calorimeter response from the potential mismodeling of threshold effects in topological clustering.	0	0-10
Neutral	The uncertainty in the calorimeter response to neutral hadrons based on studies of physics model variations.	0	5-10
K_L	An additional uncertainty in the response to neutral K_L in the calorimeter based on studies of physics model variations.	0	20
E/p Misalignment	The uncertainty in the p measurement from misalignment of the ID.	0	1
Hadrons, $p > 350$ GeV	A flat uncertainty for all particles above the energy range or outside the longitudinal range probed with the combined test beam.	0	10

Table 1: The dominant sources of corrections and systematic uncertainties in the [JES](#) estimation technique, including typical values for the correcting shift (Δ) and the associated uncertainty (σ).

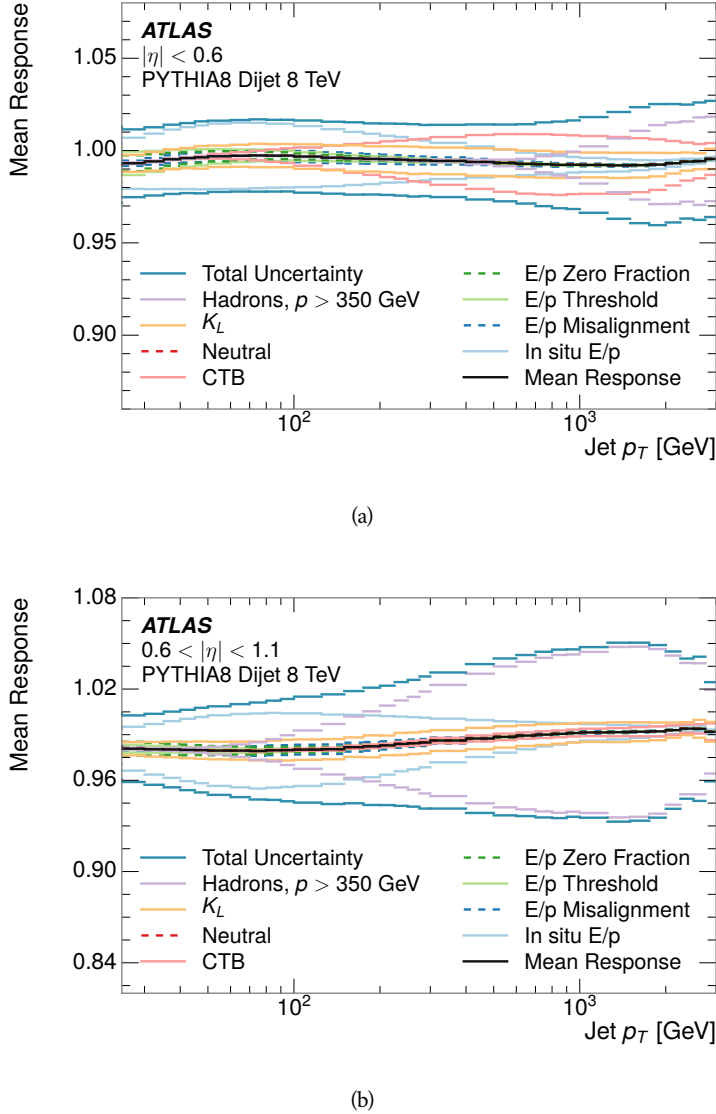


Figure 20: The [JES](#) uncertainty contributions, as well as the total [JES](#) uncertainty, as a function of jet p_T for (a) $|\eta| < 0.6$ and (b) $0.6 < |\eta| < 1.1$.

745 9.3 SUMMARY

746 The technique described above provides a jet energy scale and uncertainty by
 747 building up jet corrections from the energy deposits of constituent particles. The
 748 E/p measurements are crucial in providing corrections for the majority of parti-
 749 cles in the jets. The uncertainty derived this way is between 2 and 5% and is about
 750 twice as large at corresponding momentum than jet balance methods. However
 751 this is the only uncertainty available for very energetic jets using 2012 data and
 752 simulation, and repeating this method with Run 2 data and simulation will be
 753 important in providing an uncertainty for the most energetic jets in 13 TeV col-
 754 lisions.

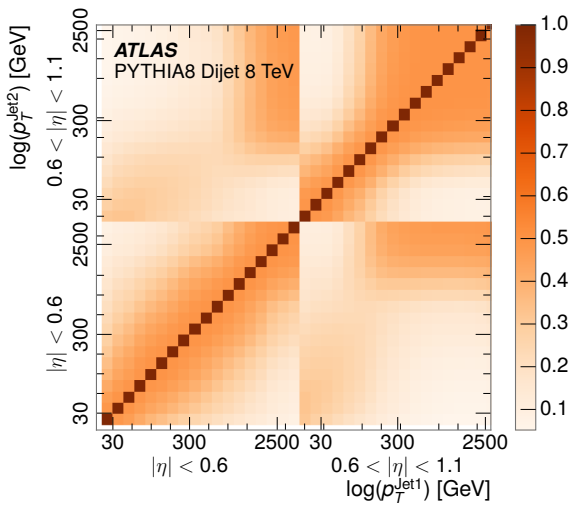


Figure 21: The JES correlations as a function of jet p_T and $|\eta|$ for jets in the central region of the detector.

755

PART V

756

SEARCH FOR LONG-LIVED PARTICLES

757

You can put some informational part preamble text here.

10

758

759 LONG-LIVED PARTICLES IN ATLAS

760 10.1 OVERVIEW AND CHARACTERISTICS

761 10.2 SIMULATION

762

763 EVENT SELECTION

764 The **LLP!** (**LLP!**s targeted by this search differ in their interactions with the de-
 765 tector from other, **SM** particles primarily because of their large mass. That large
 766 mass results in a low β when produced at the energies available at the **LHC**, and
 767 such slow-moving particles heavily ionize in detector material when charged.
 768 Each layer of the pixel detector provides a measurement of that ionization, through
 769 time over threshold (**ToT**), as discussed in Section 6.3.1. The ionization in the
 770 pixel detector, quantified in terms of dE/dx , provides the major focus for this
 771 search technique, both because of its discriminating power and also because of
 772 the large range of lifetimes where it can be used.

773 The dE/dx variable needs to be augmented with a few additional selection
 774 requirements to form a complete search. Ionization is not currently available in
 775 any form during triggering, so this search instead relies on E_T^{miss} to trigger the
 776 events out of necessity. Although triggering on E_T^{miss} is not particularly efficient,
 777 E_T^{miss} is often large for many production mechanisms of **LLP!**s, as discussed in
 778 Section 10.1.

779 Ionization is most effective in rejecting backgrounds for well-measured, high-
 780 momentum tracks, so some basic requirements on quality and kinematics are
 781 placed on the particles considered in this search. In particular a newly introduced
 782 tracking variable (referred to as N_{SS} and defined in detail in Section 11.2) is very
 783 effective in removing highly-ionizing backgrounds caused by overlapping tracks.
 784 A few additional requirements are placed on the tracks considered for **LLP!** candi-
 785 dates that increase background rejection by targeting specific types of **SM** parti-
 786 cles (Section 11.3). These techniques provide a significant analysis improvement
 787 over previous iterations of ionization-based searches on ATLAS by providing
 788 additional background rejection with minimal loss in signal efficiency.

789 The ionization measurement with the Pixel detector can be calibrated to pro-
 790 vide an estimator of $\beta\gamma$. $\beta\gamma$, together with the momentum measurement pro-
 791 vided by tracking, can be used to reconstruct a mass for each track which tra-
 792 verses the pixel detector. That mass variable will be peaked at the **LLP!** mass for
 793 any signal, and provides an additional tool to search for an excess. In addition
 794 to an explicit requirement on ionization, this search constructs a mass-window
 795 for each targeted mass range in order to evaluate any excess of events and to
 796 set limits. Construction, calibration, and requirements for the mass variable are
 797 discussed in Section 11.4.2.

798 11.1 TRIGGER

799 11.2 KINEMATICS AND ISOLATION

800 11.3 STANDARD MODEL REJECTION

801 11.4 IONIZATION

802 11.4.1 DE/DX CALIBRATION

803 11.4.2 MASS ESTIMATION

12

804

805 BACKGROUND ESTIMATION

806 12.1 BACKGROUND SOURCES

807 12.2 PREDICTION METHOD

808 12.3 VALIDATION AND UNCERTAINTY

13

809

810 SYSTEMATIC UNCERTAINTIES AND RESULTS

811 13.1 SYSTEMATIC UNCERTAINTIES

812 13.2 FINAL YIELDS

14

813

814 INTERPRETATION

815 14.1 CROSS SECTIONAL LIMITS

816 14.2 MASS LIMITS

817 14.3 CONTEXT FOR LONG-LIVED SEARCHES

818

PART VI

819

CONCLUSIONS

820

You can put some informational part preamble text here.

15

821

822 SUMMARY AND OUTLOOK

823 15.1 SUMMARY

824 15.2 OUTLOOK

825

PART VII

826

APPENDIX

827

828

829 INELASTIC CROSS SECTION

A

B

830

831 APPENDIX TEST

832 Examples: *Italics*, SMALL CAPS, ALL CAPS ¹. Acronym testing: **UML!** (**UML!**) –
833 **UML! – UML! (UML!) – UML!s**

This appendix is temporary and is here to be used to check the style of the document.

834 B.1 APPENDIX SECTION TEST

835 Random text that should take up a few lines. The purpose is to see how sections
836 and subsections flow with some actual context. Without some body copy be-
837 tween each heading it can be difficult to tell if the weight of the fonts, styles,
838 and sizes use work well together.

839 B.1.1 APPENDIX SUBECTION TEST

840 Random text that should take up a few lines. The purpose is to see how sections
841 and subsections flow with some actual context. Without some body copy be-
842 tween each heading it can be difficult to tell if the weight of the fonts, styles,
843 and sizes use work well together.

844 B.2 A TABLE AND LISTING

845 Curabitur tellus magna, porttitor a, commodo a, commodo in, tortor. Donec in-
846 terdum. Praesent scelerisque. Maecenas posuere sodales odio. Vivamus metus la-
847 cus, varius quis, imperdiet quis, rhoncus a, turpis. Etiam ligula arcu, elementum a,
848 venenatis quis, sollicitudin sed, metus. Donec nunc pede, tincidunt in, venenatis
849 vitae, faucibus vel, nibh. Pellentesque wisi. Nullam malesuada. Morbi ut tellus ut
850 pede tincidunt porta. Lorem ipsum dolor sit amet, consectetur adipiscing elit.
851 Etiam congue neque id dolor.

852 There is also a Python listing below Listing 1.

1 Footnote example.

LABITUR BONORUM PRI NO	QUE VISTA	HUMAN
fastidii ea ius	germano	demonstratea
suscipit instructior	titulo	personas
quaestio philosophia	facto	demonstrated

Table 2: Autem usu id.

853 B.3 SOME FORMULAS

Due to the statistical nature of ionisation energy loss, large fluctuations can occur in the amount of energy deposited by a particle traversing an absorber element². Continuous processes such as multiple scattering and energy loss play a relevant role in the longitudinal and lateral development of electromagnetic and hadronic showers, and in the case of sampling calorimeters the measured resolution can be significantly affected by such fluctuations in their active layers. The description of ionisation fluctuations is characterised by the significance parameter κ , which is proportional to the ratio of mean energy loss to the maximum allowed energy transfer in a single collision with an atomic electron:

You might get unexpected results using math in chapter or section heads.
Consider the pdfspacing option.

$$\kappa = \frac{\xi}{E_{\max}} \quad (1)$$

E_{\max} is the maximum transferable energy in a single collision with an atomic electron.

$$E_{\max} = \frac{2m_e\beta^2\gamma^2}{1 + 2\gamma m_e/m_x + (m_e/m_x)^2},$$

854 where $\gamma = E/m_x$, E is energy and m_x the mass of the incident particle, $\beta^2 =$
 855 $1 - 1/\gamma^2$ and m_e is the electron mass. ξ comes from the Rutherford scattering
 856 cross section and is defined as:

$$\xi = \frac{2\pi z^2 e^4 N_{Av} Z \rho \delta x}{m_e \beta^2 c^2 A} = 153.4 \frac{z^2}{\beta^2} \frac{Z}{A} \rho \delta x \text{ keV},$$

857 where

858 z charge of the incident particle
 859 N_{Av} Avogadro's number
 860 Z atomic number of the material
 861 A atomic weight of the material
 862 ρ density
 δx thickness of the material
 859 κ measures the contribution of the collisions with energy transfer close to
 860 E_{\max} . For a given absorber, κ tends towards large values if δx is large and/or if
 861 β is small. Likewise, κ tends towards zero if δx is small and/or if β approaches
 862 1.

2 Examples taken from Walter Schmidt's great gallery:
<http://home.vrweb.de/~was/mathfonts.html>

Listing 1: A floating example (listings manual)

```
1 for i in xrange(10):
    print i, i*i, i*i*i
print "done"
```

863 The value of κ distinguishes two regimes which occur in the description of
864 ionisation fluctuations:

- 865 1. A large number of collisions involving the loss of all or most of the incident
866 particle energy during the traversal of an absorber.

867 As the total energy transfer is composed of a multitude of small energy
868 losses, we can apply the central limit theorem and describe the fluctua-
869 tions by a Gaussian distribution. This case is applicable to non-relativistic
870 particles and is described by the inequality $\kappa > 10$ (i. e., when the mean
871 energy loss in the absorber is greater than the maximum energy transfer
872 in a single collision).

- 873 2. Particles traversing thin counters and incident electrons under any condi-
874 tions.

875 The relevant inequalities and distributions are $0.01 < \kappa < 10$, Vavilov
876 distribution, and $\kappa < 0.01$, Landau distribution.

877 BIBLIOGRAPHY

- 878 [1] ATLAS Collaboration. “The ATLAS Simulation Infrastructure”. In: *Eur.*
879 *Phys. J. C* 70 (2010), p. 823. doi: [10.1140/epjc/s10052-010-1429-9](https://doi.org/10.1140/epjc/s10052-010-1429-9).
880 arXiv: [1005.4568 \[hep-ex\]](https://arxiv.org/abs/1005.4568). SOFT-2010-01.
- 881 [2] ATLAS Collaboration. “A study of the material in the ATLAS inner de-
882 tector using secondary hadronic interactions”. In: *JINST* 7 (2012), P01013.
883 doi: [10.1088/1748-0221/7/01/P01013](https://doi.org/10.1088/1748-0221/7/01/P01013). arXiv: [1110.6191 \[hep-ex\]](https://arxiv.org/abs/1110.6191).
884 PERF-2011-08.
- 885 [3] ATLAS Collaboration. *Summary of ATLAS Pythia 8 tunes*. ATL-PHYS-PUB-
886 2012-003. 2012. url: <http://cds.cern.ch/record/1474107>.
- 887 [4] ATLAS Collaboration. “Jet energy measurement with the ATLAS detector
888 in proton–proton collisions at $\sqrt{s} = 7$ TeV”. In: *Eur. Phys. J. C* 73 (2013),
889 p. 2304. doi: [10.1140/epjc/s10052-013-2304-2](https://doi.org/10.1140/epjc/s10052-013-2304-2). arXiv: [1112.6426 \[hep-ex\]](https://arxiv.org/abs/1112.6426). PERF-2011-03.
- 890 [5] ATLAS Collaboration. “Single hadron response measurement and calorime-
891 ter jet energy scale uncertainty with the ATLAS detector at the LHC”. In:
892 *Eur. Phys. J. C* 73 (2013), p. 2305. doi: [10.1140/epjc/s10052-013-2305-1](https://doi.org/10.1140/epjc/s10052-013-2305-1). arXiv: [1203.1302 \[hep-ex\]](https://arxiv.org/abs/1203.1302). PERF-2011-05.
- 893 [6] ATLAS Collaboration. “Electron and photon energy calibration with the
894 ATLAS detector using LHC Run 1 data”. In: *Eur. Phys. J. C* 74 (2014), p. 3071.
895 doi: [10.1140/epjc/s10052-014-3071-4](https://doi.org/10.1140/epjc/s10052-014-3071-4). arXiv: [1407.5063 \[hep-ex\]](https://arxiv.org/abs/1407.5063). PERF-2013-05.
- 896 [7] ATLAS Collaboration. “Jet energy measurement and its systematic uncer-
897 tainty in proton–proton collisions at $\sqrt{s} = 7$ TeV with the ATLAS detec-
898 tor”. In: *Eur. Phys. J. C* 75 (2015), p. 17. doi: [10.1140/epjc/s10052-014-3190-y](https://doi.org/10.1140/epjc/s10052-014-3190-y). arXiv: [1406.0076 \[hep-ex\]](https://arxiv.org/abs/1406.0076). PERF-2012-01.
- 899 [8] ATLAS Collaboration. “A measurement of the calorimeter response to sin-
900 gle hadrons and determination of the jet energy scale uncertainty using
901 LHC Run-1 pp -collision data with the ATLAS detector”. In: (2016). arXiv:
902 [1607.08842 \[hep-ex\]](https://arxiv.org/abs/1607.08842). PERF-2015-05.
- 903 [9] ATLAS Collaboration. “Topological cell clustering in the ATLAS calorime-
904 ters and its performance in LHC Run 1”. In: (2016). arXiv: [1603.02934 \[hep-ex\]](https://arxiv.org/abs/1603.02934).
- 905 [10] E. Abat et al. “Study of energy response and resolution of the ATLAS barrel
906 calorimeter to hadrons of energies from 20 to 350 GeV”. In: *Nucl. Instrum.*
907 *Meth. A* 621.1-3 (2010), pp. 134 – 150. doi: <http://dx.doi.org/10.1016/j.nima.2010.04.054>.

- 914 [11] P. Adragna et al. "Measurement of Pion and Proton Response and Lon-
 915 gitudinal Shower Profiles up to 20 Nuclear Interaction Lengths with the
 916 ATLAS Tile Calorimeter". In: *Nucl. Instrum. Meth. A* 615 (2010), pp. 158–
 917 181. doi: [10.1016/j.nima.2010.01.037](https://doi.org/10.1016/j.nima.2010.01.037).
- 918 [12] S. Agostinelli et al. "GEANT4: A simulation toolkit". In: *Nucl. Instrum. Meth.*
 919 A 506 (2003), pp. 250–303. doi: [10.1016/S0168-9002\(03\)01368-8](https://doi.org/10.1016/S0168-9002(03)01368-8).
- 920 [13] N. S. Amelin et al. "Transverse flow and collectivity in ultrarelativistic
 921 heavy-ion collisions". In: *Phys. Rev. Lett.* 67 (1991), p. 1523. doi: [10.1103/PhysRevLett.67.1523](https://doi.org/10.1103/PhysRevLett.67.1523).
- 923 [14] N. S. Amelin et al. "Collectivity in ultrarelativistic heavy ion collisions". In:
 924 *Nucl. Phys. A* 544 (1992), p. 463. doi: [10.1016/0375-9474\(92\)90598-E](https://doi.org/10.1016/0375-9474(92)90598-E).
- 926 [15] B. Andersson, A. Tai, and B.-H. Sa. "Final state interactions in the (nuclear)
 927 FRITIOF string interaction scenario". In: *Z. Phys. C* 70 (1996), pp. 499–
 928 506. doi: [10.1007/s002880050127](https://doi.org/10.1007/s002880050127).
- 929 [16] B. Andersson et al. "A model for low-pT hadronic reactions with general-
 930 izations to hadron-nucleus and nucleus-nucleus collisions". In: *Nucl. Phys.*
 931 B 281 (1987), p. 289. doi: [10.1016/0550-3213\(87\)90257-4](https://doi.org/10.1016/0550-3213(87)90257-4).
- 932 [17] H. W. Bertini and P. Guthrie. "News item results from medium-energy
 933 intranuclear-cascade calculation". In: *Nucl. Instr. and Meth. A* 169 (1971),
 934 p. 670. doi: [10.1016/0375-9474\(71\)90710-X](https://doi.org/10.1016/0375-9474(71)90710-X).
- 935 [18] L. V. Bravin et al. "Scaling violation of transverse flow in heavy ion col-
 936 lisions at AGS energies". In: *Phys. Lett. B* 344 (1995), p. 49. doi: [10.1016/0370-2693\(94\)01560-Y](https://doi.org/10.1016/0370-2693(94)01560-Y).
- 938 [19] L. V. Bravina et al. "Fluid dynamics and Quark Gluon string model - What
 939 we can expect for Au+Au collisions at 11.6 AGeV/c". In: *Nucl. Phys. A* 566
 940 (1994), p. 461. doi: [10.1016/0375-9474\(94\)90669-6](https://doi.org/10.1016/0375-9474(94)90669-6).
- 941 [20] CMS Collaboration. "The CMS barrel calorimeter response to particle
 942 beams from 2 to 350 GeV/c". In: *Eur. Phys. J. C* 60.3 (2009). doi: [10.1140/epjc/s10052-009-0959-5](https://doi.org/10.1140/epjc/s10052-009-0959-5).
- 944 [21] H. S. Fesefeldt. *GHEISHA program*. Pitha-85-02, Aachen. 1985.
- 945 [22] G. Folger and J.P. Wellisch. "String parton models in Geant4". In: (2003).
 946 arXiv: [nucl-th/0306007](https://arxiv.org/abs/nucl-th/0306007).
- 947 [23] B. Ganhuyag and V. Uzhinsky. "Modified FRITIOF code: Negative charged
 948 particle production in high energy nucleus nucleus interactions". In: *Czech.
 949 J. Phys.* 47 (1997), pp. 913–918. doi: [10.1023/A:1021296114786](https://doi.org/10.1023/A:1021296114786).
- 950 [24] M. P. Guthrie, R. G. Alsmiller, and H. W. Bertini. "Calculation of the cap-
 951 ture of negative pions in light elements and comparison with experiments
 952 pertaining to cancer radiotherapy". In: *Nucl. Instrum. Meth.* 66 (1968), pp. 29–
 953 36. doi: [10.1016/0029-554X\(68\)90054-2](https://doi.org/10.1016/0029-554X(68)90054-2).
- 954 [25] J. Beringer et al. (Particle Data Group). "Review of Particle Physics". In:
 955 *Chin. Phys. C* 38 (2014), p. 090001. URL: <http://pdg.lbl.gov>.

- 956 [26] V.A. Karmanov. "Light Front Wave Function of Relativistic Composite
957 System in Explicitly Solvable Model". In: *Nucl. Phys. B* 166 (1980), p. 378.
958 doi: [10.1016/0550-3213\(80\)90204-7](https://doi.org/10.1016/0550-3213(80)90204-7).
- 959 [27] Hung-Liang Lai, Marco Guzzi, Joey Huston, Zhao Li, Pavel M. Nadolsky,
960 et al. "New parton distributions for collider physics". In: *Phys. Rev. D* 82
961 (2010), p. 074024. doi: [10.1103/PhysRevD.82.074024](https://doi.org/10.1103/PhysRevD.82.074024). arXiv: [1007.2241 \[hep-ph\]](https://arxiv.org/abs/1007.2241).
- 963 [28] A.D. Martin, W.J. Stirling, R.S. Thorne, and G. Watt. "Parton distributions
964 for the LHC". In: *Eur. Phys. J. C* 63 (2009). Figures from the [MSTW Website](#),
965 pp. 189–285. doi: [10.1140/epjc/s10052-009-1072-5](https://doi.org/10.1140/epjc/s10052-009-1072-5). arXiv: [0901.0002](https://arxiv.org/abs/0901.0002).
- 967 [29] B. Nilsson-Almqvist and E. Stenlund. "Interactions Between Hadrons and
968 Nuclei: The Lund Monte Carlo, Fritiof Version 1.6". In: *Comput. Phys. Com-*
969 *mun.* 43 (1987), p. 387. doi: [10.1016/0010-4655\(87\)90056-7](https://doi.org/10.1016/0010-4655(87)90056-7).
- 970 [30] A. Ribon et al. *Status of Geant4 hadronic physics for the simulation of LHC*
971 *experiments at the start of LHC physics program.* CERN-LCGAPP-2010-02.
972 2010. URL: <http://lcgapp.cern.ch/project/docs/noteStatusHadronic2010.pdf>.
- 974 [31] A. Sherstnev and R.S. Thorne. "Parton Distributions for LO Generators".
975 In: *Eur. Phys. J. C* 55 (2008), pp. 553–575. doi: [10.1140/epjc/s10052-008-0610-x](https://doi.org/10.1140/epjc/s10052-008-0610-x). arXiv: [0711.2473](https://arxiv.org/abs/0711.2473).
- 977 [32] T. Sjöstrand, S. Mrenna, and P. Skands. "A Brief Introduction to PYTHIA
978 8.1". In: *Comput. Phys. Commun.* 178 (2008), pp. 852–867. doi: [10.1016/j.cpc.2008.01.036](https://doi.org/10.1016/j.cpc.2008.01.036). arXiv: [0710.3820](https://arxiv.org/abs/0710.3820).
- 980 [33] Peter Speckmayer. "Energy Measurement of Hadrons with the CERN AT-
981 LAS Calorimeter". Presented on 18 Jun 2008. PhD thesis. Vienna: Vienna,
982 Tech. U., 2008. URL: <http://cds.cern.ch/record/1112036>.

983 DECLARATION

984 Put your declaration here.

985 *Berkeley, CA, September 2016*

986

Bradley Axen

987

988 COLOPHON

989

Not sure that this is necessary.